GEOPHYSICS, VOL. 90, NO. 4 (JULY-AUGUST 2025); P. G139–G150, 11 FIGS., 2 TABLES.
10.1190/GEO2024-0312.1

AeroVmag: A new aero-towed vector magnetometer system

Sergei Freiman[1] and Roi Granot[1]

ABSTRACT

Magnetic fields are vectorial in nature, yet most geophysical surveys measure the amplitude of the fields, resulting in total field magnetic anomalies. This tradition is motivated mainly by the ease with which total field measurements can be conducted and the technical challenges involved in the acquisition of vector measurements. The quality of vector magnetometer systems depends mainly on the accuracy with which the orientation (i.e., pitch, roll, and yaw angles) is known. To overcome this challenge, triaxial vector magnetometers are commonly installed onto the platforms that carry these systems (e.g., ships and airplanes), which causes temporally varying magnetic contamination that is difficult to eliminate and quantify. We develop the first aero-towed vector magnetometer system, called AeroVmag, which can measure the three components of the magnetic field with negligible magnetic contamination induced by the carrying platform. The system contains a dual global navigation satellite system/inertial navigation system coupled with triaxial and scalar magnetometers. We test the system near the central Dead Sea Fault system in northern Israel, where we collected a dense grid of data approximately 110 m above the surface. We use crossover analysis to show that the system yields internally consistent data with noise levels of 15.6/44.5/14.0 nT for the north/east/vertical components, respectively. We show that these noise levels arise from the uncertainties related to the orientation of the towed bird, indicating that our processing scheme mitigates any other magnetic contamination or biases. The test survey results compare favorably with the existing sea surface total field anomalies and with the seismic reflection data, thus demonstrating the reliability of the system. The AeroVmag system can be towed by helicopters, fixed-wing aircraft, and heavy-lifting drones, providing obvious operational and economic benefits. Its applicability is expected to be highest in equatorial and regional surveys that study crustal-scale phenomena or when characterizing off-profile sources.

INTRODUCTION

Magnetic field measurements provide essential constraints for geodynamic, environmental, and exploration studies (e.g., Nabighian et al., 2005; Gee and Kent, 2007; Hinze et al., 2013). Despite the vectorial nature of magnetic fields, technical limitations have traditionally restricted marine and continental surveys to measuring only the magnitude of the local magnetic fields, and those measurements are then used to calculate total field magnetic anomalies. Under the assumption that the induced crustal magnetic fields are significantly smaller than the ambient geomagnetic field, these total field anomalies represent the component of the locally induced magnetic fields projected in the direction of the ambient geomagnetic field (Blakely, 1995). In the case of strong magnetization and/or a thick magnetic source layer, however, the calculated total field anomalies may deviate significantly from the true magnetic anomaly (Kontis and Young, 1964; Yang et al., 2020). Furthermore, for equatorial magnetized bodies oriented along a north–south direction, the total field anomalies are relatively small, and they tend to be contaminated by strong diurnal variations caused by the equatorial electrojets (Rigoti et al., 2000; Gee and Cande, 2002). Together, these characteristics prevent total field magnetic anomalies from being identified for equatorial north–south magnetized bodies (e.g., north-trending dikes). Because of that, for instance, the crustal ages of the equatorial Atlantic and Pacific basins are mostly unknown (Horner-Johnson and Gordon, 2003; Seton et al., 2014). Finally, when collecting the total field data, the azimuth and structures of the magnetic boundaries can only be deduced by collecting multiple profiles across the boundaries (e.g., Seama et al., 1993; Blakely, 1995). However, vector magnetic anomalies may help overcome these limitations.

Manuscript received by the Editor 16 May 2024; revised manuscript received 23 January 2025; published ahead of production 24 March 2025; published online 10 June 2025.
[1]Ben-Gurion University of the Negev, Department of Earth and Environmental Sciences, Beer-Sheva, Israel. E-mail: freimansgy@gmail.com; rgranot@bgu.ac.il (corresponding author).

DOI:10.1190/geo2024-0312.1

In equatorial regions, for north-striking bodies, the magnitudes of the vertical and horizontal magnetic anomalies are approximately 10 times larger compared with the total field anomalies (Gee and Cande, 2002). Therefore, despite the relatively strong equatorial diurnal magnetic fluctuations that tend to be concentrated within the horizontal field (Yamazaki and Maute, 2017), the anomalous three components there are resolvable and, thus, allow for reliable magnetic interpretation (Horner-Johnson and Gordon, 2003; Barckhausen et al., 2008; Engels et al., 2008). Vector anomalies also accurately represent the crustal magnetic fields, regardless of the strength of the magnetization and the thickness of the source layer, which, if strong and thick, may spoil the underlying assumption that the anomalous magnetic fields are much smaller than the ambient geomagnetic field (e.g., Yang et al., 2020). Furthermore, vector anomalies also allow for the strike orientation and dimensionality (i.e., large-scale 2D lineated sources versus nonlineated 3D sources) of the magnetic source layer to be estimated using data from a single profile (Seama et al., 1993; Korenaga, 1995; Granot, 2016). Despite these obvious benefits, vector magnetic measurements have typically suffered from significant imprecisions because they require accurate orientation knowledge. Furthermore, their analysis requires relatively extensive processing procedures and, as a result, they have rarely been acquired.

Aerial vector data have traditionally been collected using magnetometers installed onboard the aerial platforms (Blakely et al., 1973; Coleman, 1992; Dransfield et al., 2003; Isezaski and Matsuo, 2009; Xie et al., 2020). The orientation of these systems is constrained by the inertial navigation system (INS) of the carrying platforms, but besides the uncertainties related to the INS, they also suffer from considerable, temporally varying magnetic contamination induced by the carrying platform, which is difficult to eliminate and quantify. Unfortunately, none of these published works has thoroughly documented the noise levels induced by the carrying platform, the sensor (e.g., heading errors), the INS, and those induced by diurnal external field variations.

Vector magnetometers have also been installed onboard marine research vessels (e.g., Isezaki, 1986; Seama et al., 1993; Nogi and Kaminuma, 1999) and on autonomous underwater vehicles (e.g., Honsho et al., 2013; Berrios-Rivera et al., 2023). Similar to the aerial vector systems, these marine installations suffer from time-dependent magnetic contamination induced by the carrying platform that can introduce significant bias and drift into the calculated vector anomalies (Korenaga, 1995). To avoid this bias, the aerial and marine vector data need to be balanced and filtered for the long wavelength signal (approximately $>10^2$ s). On the other hand, towed marine sea surface and deep-towed vector magnetometer systems lack the magnetic contamination induced by the towing platform, yet their heading directions are poorly constrained (Gee and Cande, 2002; Yamamoto et al., 2005; Kato et al., 2007; Engels et al., 2008). Thus, these towed marine systems effectively provide reliable knowledge about only the horizontal and vertical components of the anomalous field.

The recent technological development of a miniature coupled global navigation satellite system (GNSS) with an INS provides remarkably improved constraints (<0.1° accuracy for the pitch, roll, and yaw angles) of the orientations of aerial systems (Jekeli, 2023). Here, we introduce the first aero-towed vector magnetometer system, called AeroVmag, that exploits this new generation of orientation devices to provide fully oriented vector magnetic data that are virtually free of magnetic contamination induced by the towing platform. The system is designed to be towed by either fixed-wing or rotary-wing (i.e., helicopters and heavy-lifting drones) aircraft, which allows for operational flexibility and boasts lower per-kilometer survey costs. The relatively high velocity of the carrying platforms essentially separates the typical wavelength of the geologically related anomalies (approximately 10^0–10^1 km) from the wavelength related to the diurnal variations of the external magnetic fields (approximately 10^3–10^4 km), making the separation of the diurnal variations from the geologically related magnetic signal rather straightforward (e.g., Horner-Johnson and Gordon, 2003). We conducted a test survey in northern Israel over the northeastern part of the Sea of Galilee and across the adjacent, onshore central Dead Sea Fault system. The results allow us to assess the reliability of the system and to infer new geologic insights about the structure of the central Dead Sea Fault. In the following, we describe the AeroVmag system and the calibration and processing procedure that we performed. We then present the results of the test survey and discuss the reliability and limitations of the system, as well as the tectonic implications of the results.

AEROVMAG: AN AERO-TOWED VECTOR MAGNETOMETER SYSTEM

The AeroVmag system (Figure 1) consists of triaxial and scalar total field magnetometers, a dual antenna GNSS-aided INS orientation sensor, and a microprocessor device. All sensors and electronics were fixed on a rigid, composite glass fiber baseplate (Apexfiber Ltd). After conducting a series of laboratory tests, the magnetometers were placed so that the internal magnetic noise produced by the other electrical components was lower than 0.5 nT. We measure the three components of the magnetic field using a digital triaxial ring core fluxgate magnetometer (MFG-1S of Magson GmbH). For redundancy, we also measure the amplitude of the magnetic field using a rubidium optically pumped magnetometer (QTFM of Quspin). The specifications of the magnetometers are shown in Table 1.

The position (location and altitude), orientation information (i.e., pitch, roll, and yaw angles), and time are provided by the GNSS/INS VN-300 device of VectorNav. The data are internally synced and transmitted live to the operating personnel via a 40 m tow rope (Figure 1c). The length of the towing rope ensures that the carrying platform has a negligible influence (i.e., magnetic contamination) on the measured magnetic signal. If carried by smaller platforms, such as heavy-lifting drones, the length of the rope could be shortened. Overall, with a 40 m tow rope, it is safe to operate the system as long as sharp maneuvers are avoided. The rope is made from braided ultra-high molecular weight polyethylene fibers (giving an overall diameter of 2 cm) and has a breaking load of 11 tons. All data are saved internally and externally on the operating computer. The tow rope contains seven conducting wires for the transmission of the power supply from the carrying platform (12 V direct current with a consumption of 0.7 A), real-time control, and live data transmission. The system is hosted within the Lake Central Air Services (LCAS) towed bird setup, which altogether weighs 27 kg. The strength of the tow rope and the external design of the bird allow the system to be towed under a large range of dynamic conditions (i.e., velocity and acceleration), and thus, it can be operated by various fixed- and rotary-wing platforms.

The VN-300 position and orientation device comprises a GNSS sensor (using the GPS, Galileo, and SBAS satellite constellations) outfitted with two antennas, installed 2 m apart for optimal performance. It also includes an INS system comprising triaxial digital

gyros, triaxial accelerometers, and triaxial magnetometers. The measurements from these three sensors are internally fused using a Kalman filter, providing a drift-free, high-rate orientation solution. The VN-300 exhibits a horizontal positional accuracy of one meter root mean square error (RMSE) and a vertical accuracy of 1.5 m RMSE. Under dynamic yet stable conditions (i.e., no significant accelerations or rotations), the attitude accuracy of the sensor is approximately 0.03° 1σ error for the pitch and roll angles and up to 0.08° RMSE for the yaw angle. System accuracy is inversely related to the angular rotation speed at which it is operated. The yaw angle is most sensitive to the angular rotation speed, especially when sharp turns are executed.

The uncertainties of the three magnetic components obtained after the transformation to geographical coordinates depend on the uncertainties in bird attitude (i.e., 0.03°/0.03°/0.08° for the pitch/roll/yaw angles) and the strength and direction of the ambient geomagnetic field. Thus, at the level of accuracy of the VN-300, the theoretical random noise of the north, east, and vertical components of the anomalous magnetic field ranged globally between approximately 1 and 75 nT (Figure 2). These theoretical noise levels were calculated using a synthetic data set of 1000 uniformly distributed attitude triplets (pitch, roll, and yaw). The international geomagnetic reference field (IGRF) (Alken et al., 2021) was used for each 5° grid cell. We rotated the components of the local IGRF using these attitude triplets to obtain the "true" field measured in bird orientation. We then added the angular noise generated by the orientation sensor and rotated the "measured" components back to the geographical coordinates. The comparison (i.e., RMSE) between the resultant magnetic components and the initial IGRF values is shown in Figure 2. To evaluate the AeroVmag reliability and operational efficiency under real field conditions, we conducted a test magnetic survey near the central Dead Sea Fault system in northern Israel.

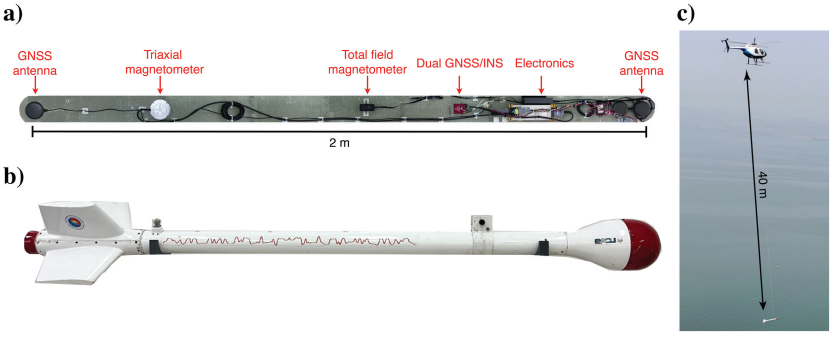

Figure 1. The AeroVmag vector magnetometer system. (a) The internal view of the system illustrates the baseplate, which houses the fluxgate triaxial magnetometer, the dual GNSS-aided INS VN-300 position and orientation sensor, and the total field QTFM magnetometer. These components, along with the baseplate and associated electronics, are enclosed within (b) the LCAS towed bird system, which is towed by (c) a single, 40 m long rope.

Table 1. Specifications for the triaxial and total field magnetometers.

	MFG-1S (Magson)	QTFM (Quspin)
Type	Triaxial ring core fluxgate	Optically pumped scalar rubidium
Sensitivity (pT)	$<15/\sqrt{Hz}$	$<1/\sqrt{Hz}$
Resolution (nT)	0.0077	NA
Long-term stability (nT/year)	<10	NA
Dynamic range (nT)	±65000	1000–100,000
Sampling rate (Hz)	up to 100	up to 400
Heading error (nT)	NA	<3

TEST SURVEY

We tested our new vector magnetometer system in March 2023 during a survey conducted over the northeastern part of the Sea of Galilee and the adjacent central section of the Dead Sea Fault system in northern Israel (Figure 3). Due to the limited total field magnetic anomaly coverage of the area, in addition to validating the system, our results add new constraints to the structural setting of the Dead Sea Fault system that straddles the survey area.

The Dead Sea Fault system is a major sinistral continental transform fault that has accommodated motion between the Sinai Microplate and the Arabian Plate since the Miocene (Garfunkel et al.,

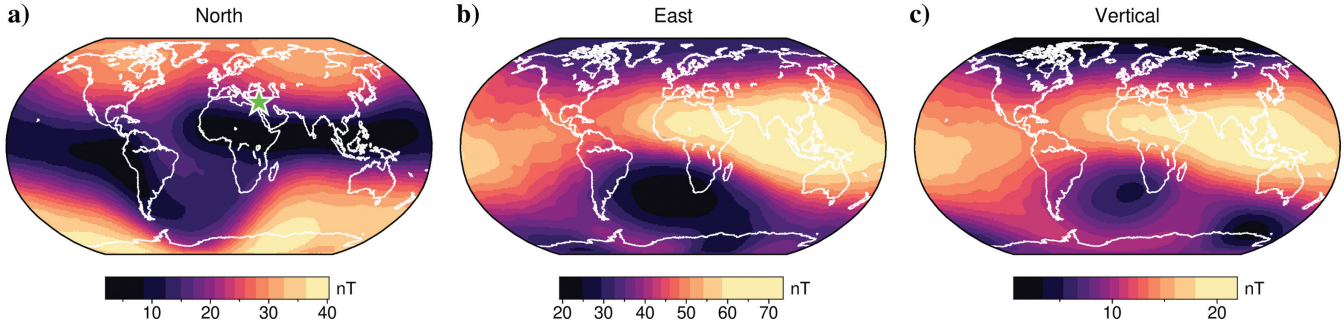

Figure 2. Theoretical noise levels (i.e., RMSE) of the (a) north, (b) east, and (c) vertical magnetic components. These predicted noise levels were calculated by considering the accuracies of the three orientation angles measured by the VN-300 sensor (0.03°/0.03°/0.08° for the pitch/roll/yaw angles, respectively) and the strength and direction of the ambient geomagnetic field. The green star in (a) indicates the location of the test survey.

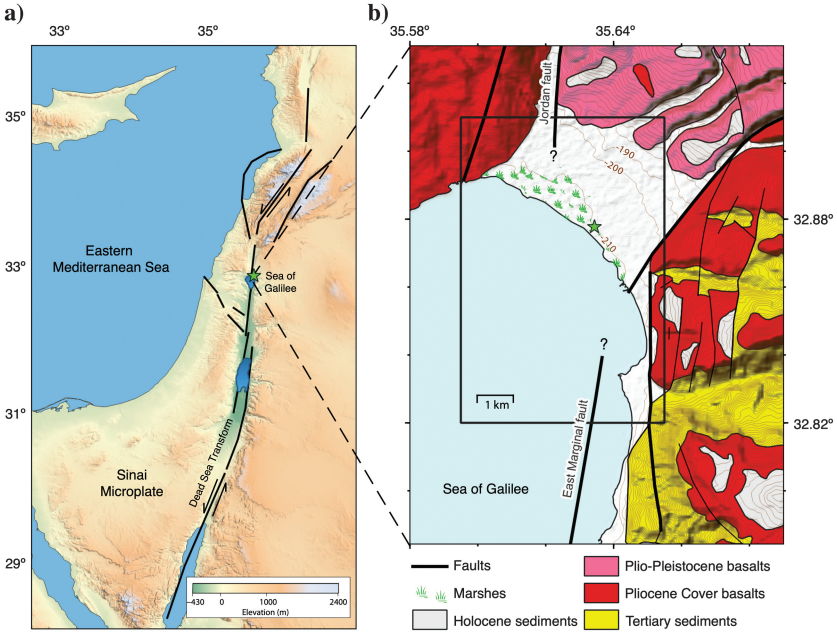

Figure 3. Test survey area. (a) Regional tectonic setting of the Dead Sea Fault system. The green star highlights the test survey location. (b) Geologic map of the study area. The black rectangle marks the location of our magnetic survey. The question marks highlight the uncertainties related to the exact position of the faults and, thus, to the exact structure of the stepover. The digital elevation model is based on SRTM data (Farr et al., 2007).

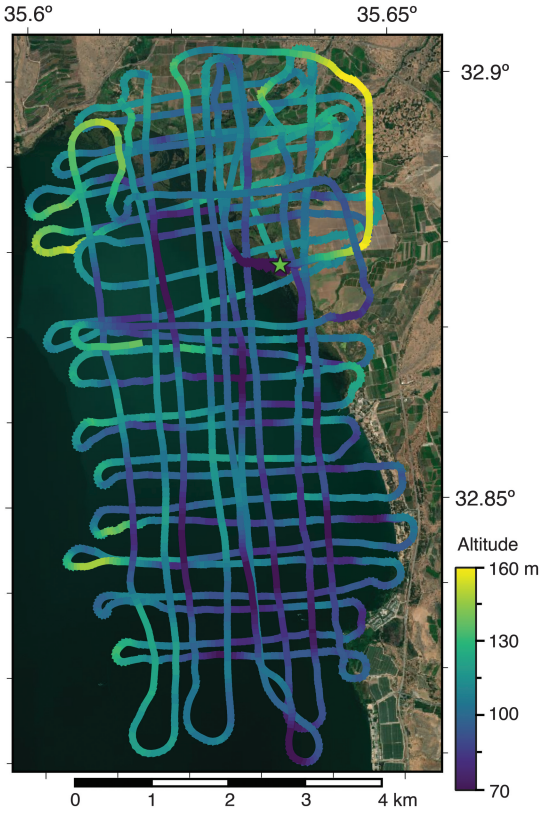

Figure 4. Flight track. The track is colored according to the altitude of the bird above the surface. The green star highlights the position of the magnetic base station.

1981; Nuriel et al., 2017) (Figure 3a). Previous geophysical works (e.g., Hurwitz et al., 2002; Reznikov et al., 2004; Gasperini et al., 2020; Hamiel and Piatibratova, 2023; ten Brink et al., 2023) suggest that the activity of the fault system has been, and still is, concentrated mainly offshore along the Eastern Marginal Fault in the Sea of Galilee (Figure 3b). North of the lake, the activity has been concentrated along the Jordan Gorge Fault (JGF) (Hurwitz et al., 2002; Hamiel et al., 2016). A small left-stepping stepover seems to connect the two segments (the Eastern Marginal Fault with the JGF), but due to the limited seismic reflection profiles, the exact structure of the stepover and how it evolved over time are still poorly resolved (e.g., Dembo et al., 2021; ten Brink et al., 2023). The survey area is characterized by approximately 175 m of thick Pliocene basaltic lava flows (Sneh et al., 1998) that serve as the main magnetic source layer (Eppelbaum et al., 2007). The basaltic flows are widely exposed on land (Eppelbaum et al., 2007; Ben-Avraham et al., 2014). Drill holes from around the lake and seismic reflection data suggest that within the lake, west of the Eastern Marginal Fault, they are overlain by up to 2 km of Pliocene to recent terrigenous sediments (Rotstein and Bartov, 1989; Hurwitz et al., 2002). The two kilometers of vertical throw along the Eastern Marginal Fault (the western hanging block is thrown downward) creates total field anomalies of a magnitude of approximately 400 nT with an approximate wavelength of 1 km (Eppelbaum et al., 2007; Ben-Avraham et al., 2014).

We towed the AeroVmag system with an MD 500 helicopter at a typical flight speed of 27 m/s. At this speed, the tow rope slightly bent backward, and the bird trailed approximately 5 m behind the helicopter. We collected data along 212.5 km of track lines that formed a grid with an average line spacing of approximately 350 m, resulting in a coverage area of 40.5 km^2. A total of 255 survey profile intersection points were obtained. The bird was towed at an average altitude of approximately 110 m above the surface (i.e., drape mode) with variations of ± 25 m during 95% of the flight (Figure 4). The GNSS/INS system was operated at a sampling rate of 25 Hz, and the average distance between successive data points was 1.08 m. We performed eight-figure calibration maneuvers at the beginning and end of the survey. Due to technical problems with the QTFM total field magnetometer during the survey, the following results were collected by the triaxial magnetometer and compared with the sea surface total field magnetic data set previously collected by Ben-Avraham et al. (2014). Unfortunately, almost no magnetic measurements had been collected from the onshore part of our study area before the current study. Finally, we monitored the diurnal variations of the ambient magnetic field by a total field magnetometer base station (Geometrics G-856, Figure 4).

DATA PROCESSING

The data recorded by the triaxial vector magnetometer and GNSS/INS sensor were processed according to the following steps: 1)) resampling to common time steps and despiking, (2) magnetom-

eter linear calibration, (3) data rotation from the bird to geographical coordinates, and (4) calculating the deviation from the IGRF, altitude and external (i.e., diurnal) magnetic field corrections. Following is a brief description of these steps.

Resampling and despiking

The sensors acquire data at different operational frequencies; therefore, we first resampled and interpolated the data to a common frequency. The GNSS/INS sensor was operated at the lowest sampling rate (25 Hz); therefore, we used it as the reference time stamps for which we interpolated the vector magnetometer (operated at 50 Hz). The despiking of the three components of the magnetometer data was done by omitting any data that exceeded the 2 nT difference between successive measurements. Overall, the vector magnetometer showed notable stability, with only eight spikes out of a total of approximately 10^5 measurements. No outbursts of GNSS/INS angle data were observed; thus, no despiking of the orientation data was required. The yaw angle became unstable during abrupt turns taken at the end of the lines, defined when the yaw angle was changed at rates larger than 6°/s. We, therefore, omitted these orientation data from further consideration.

Calibration and compensation of vector magnetometer data

Each of the three components of the triaxial fluxgate magnetometer was calibrated to account for scalar factors, gains, and nonorthogonality (Olsen et al., 2001). The linear coefficients were found using the following formula:

$$F = S \cdot P \cdot B + O, \tag{1}$$

where F is the measured local magnetic field ($F = (F_x, F_y, F_z)^{\mathrm{T}}$), B is the true magnetic field at the magnetometer position ($B = (B_x, B_y, B_z)^{\mathrm{T}}$), S is the 3×3 diagonal matrix representing the scalar factors, and P is the 3×3 matrix, which transforms the vector data into an orthogonal coordinate system. Here, O is the triaxial offset ($O = (O_x, O_y, O_z)^{\mathrm{T}}$. The magnetic field B could be obtained by solving equation 1 as follows:

$$B = P^{-1} \cdot S^{-1} \cdot (F - O). \tag{2}$$

Although magnetic contamination by the carrying platform was minimized by towing the bird away from the carrying platform, the measured signal may still be distorted by hard iron (remanent magnetization) and soft iron (induced magnetization) effects possibly caused by the magnetized objects that are installed within the system (e.g., electronics, GNSS antennas, etc.). Munschy et al. (2007) demonstrate that the removal of these effects is essentially analogous to the calibration scheme described previously. Therefore, equation 2 can be used to simultaneously calibrate and compensate the data for possible magnetic contamination induced by the electronics. In this case, O consists of the triaxial offset and the hard iron effect, and $P \cdot S$ represents the soft iron effect and the scaling and nonorthogonality corrections.

The calibration and compensation parameters were initially determined in an isolated location in southern Israel, where temporally and spatially stable magnetic field conditions prevail. During the preflight calibration experiment, the bird was slowly rotated in all azimuthal directions, making a full circle over an 8 min period. During the experiment, the pitch and roll angles were varied by up to ±40°, such that the calibration and compensation solutions covered an angular range beyond the one observed during typical flight conditions. We compared the three components against the amplitude of the local magnetic field measured by the base station. The measured amplitudes of the field were calculated based on the vector magnetometer (i.e., $\sqrt{F_x^2 + F_y^2 + F_z^2}$), showing heading-dependent variations where the field tends to be stronger (approximately 10 nT) in the north–south direction compared with the east–west measured field (Figure 5). The measured field had a standard deviation of 6.7 nT and a mean of 44,930 nT, approximately 26 nT stronger than the mean magnetic field strength measured by the base station (Figure 5). After applying the calibration and compensation parameters to the three measured components, the standard deviation decreased to 1.67 nT, and the heading-dependent variations and the offset relative to the reference field were eliminated. These parameters (Table 2) were subsequently recalculated based on the calibration eight-figure maneuvers conducted at the beginning and end of the survey and on the crossover data from the test survey, which resulted in virtually identical calibration and compensation parameters.

Finally, we assessed the contribution of eddy currents following the method of Pang et al. (2014). Our analysis shows that eddy currents may account for up to 2.7 nT of high-frequency magnetic noise and appear to occur during sharp turns of the bird. As noted previously, we omitted the data collected during the turns due to the unstable behavior of the yaw angle. Therefore, we do not consider the effects of eddy currents further.

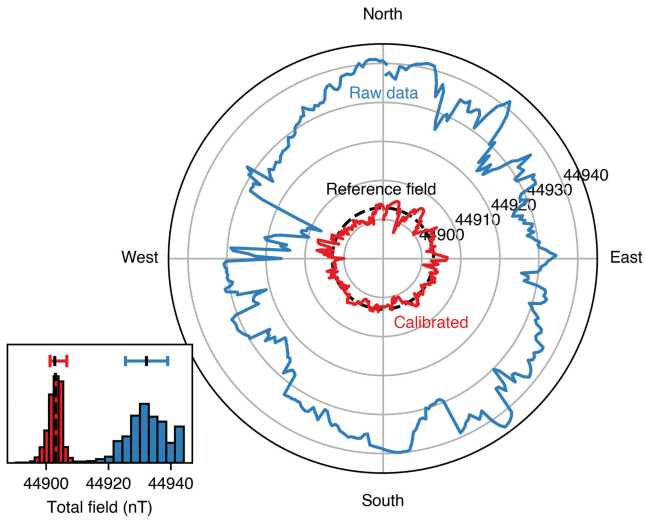

Figure 5. The calibration and compensation of the triaxial fluxgate magnetometer based on an experiment conducted under stable magnetic conditions before the test survey. The polar plot shows the strength of the measured magnetic field before (the blue line) and after (the red line) applying the calibration and compensation parameters. The total field base station data (the dashed black line) were used as the reference field. The inset histograms show the distribution of these data, whereas the horizontal lines show the standard deviations (6.7 nT prior to calibration and 1.67 nT after calibration). The black vertical lines show the mean values of these data, shifted due to the triaxial offset term (i.e., O in equation 2).

Untilting and correction for misalignment

To untilt the calibrated component data obtained from the bird to their geographical coordinates, any misalignment between the coordinate systems of the triaxial magnetometer and the GNSS/INS sensor must be taken into account. Together with misalignment correction, the formula for the rotation of the magnetic data to the geographical coordinates becomes

$$\begin{bmatrix} B_N \\ B_E \\ B_V \end{bmatrix} = R_M \cdot R_G \cdot \begin{bmatrix} B_x \\ B_y \\ B_z \end{bmatrix}, \quad (3)$$

where $B_{N,E,V}$ are the magnetic components in geographical coordinates; $B_{x,y,z}$ are the x, y, and z components of the calibrated and compensated magnetic field; R_G is the rotation matrix calculated individually for each sample based on the VN-300 recorded pitch, roll and yaw angles; and R_M is a constant 3×3 rotation matrix (i.e., misalignment information) that translates the vector magnetometer data to the bird (i.e., the GNSS/INS sensor) reference frame. We determined the misalignment rotation matrix (R_M) by minimizing the χ^2-misfit between the calibrated and untilted vector components and the components of the IGRF (Alken et al., 2021):

Table 2. Estimated calibration parameters.

	X	Y	Z
Offset (nT)	2.23875	−10.42852	17.36878
Scale	1.00079	1.00079	1.00026
Nonorthogonality (°)	0.007	−0.013	0.005

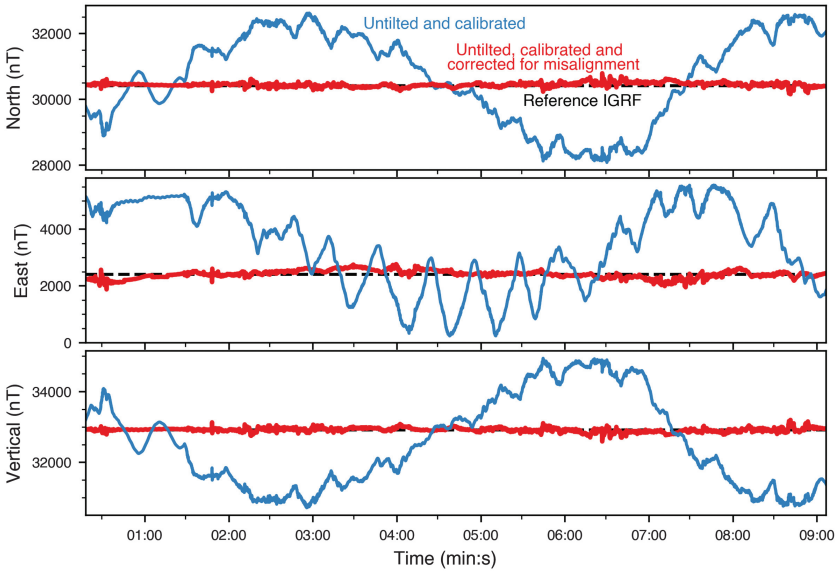

Figure 6. The effect of misalignment between the coordinate system of the triaxial magnetometer and the VN-300 orientation sensor. The blue lines represent the calibrated and compensated components of the magnetic field, rotated to the geographical coordinates. The red lines show the same data corrected for misalignment using the R_M matrix. The dashed black lines represent the IGRF components used as a reference.

$$\chi^2 = \sum \left(\frac{(B_N - N)^2 + (B_E - E)^2 + (B_V - V)^2}{3} \right), \quad (4)$$

where N, E, and V denote the components of the IGRF. We dictated the misalignment matrix only once, during the preflight ground calibration experiment, in which we assumed that the reference magnetic field remained constant. By correcting for the misalignment, we decreased the mean variations of the north/east/vertical components from 1357/1444/1442 nT to 34.4/98/34.2 nT, respectively (Figure 6). These noise levels exceed those predicted by the theoretical model (Figure 2). This experiment was conducted under static conditions, and as such, the orientation uncertainties tend to be slightly higher, which may be the reason for the higher than expected noise levels obtained.

IGRF, altitude correction, diurnal, and leveling

We reduced the calibrated, compensated, and rotated data to anomalous components using the IGRF model (Alken et al., 2021). We then upward continued the anomalies to a constant horizontal level (135 m above the water level) using the approach of Guspí (1987). This method includes low-pass filtering of the data (400 m wavelength), and therefore, no further filtering was done. There was no nearby geomagnetic station to constrain the temporal variations of the three components of the ambient magnetic field during the test flight, and as such, we used the total field base station and crossover differences to assess and correct for these possible variations. We note that the total field base station measurements indicate that variations of up to 10 nT in the strength of the ambient magnetic field occurred during the aerial survey. Our final step included the leveling of each of the three components. The longest profile collected during the survey was acquired during five minutes of flight, which is much shorter than the typical wavelength of the external field diurnal variations. Therefore, we applied the leveling approach presented by Prince and Forsyth (1984), according to which each component along each profile was assigned a single offset value that minimized the crossover differences.

RESULTS

Data collected along a representative profile (Figure 7) show the characteristic aerodynamic behavior of the towing bird and the observed three magnetic components and total field anomalies. The profile extends eastward over the lake and ends a few hundred meters beyond the coastline. Because the helicopter was flown manually and to maintain the planned course, repeated changes in the flight azimuth resulted in periodicities of approximately 10 to 15 s (i.e., approximately 250 to 400 m in wavelength) in the heading and roll angles (Figure 7f and 7g). Atmospheric conditions and altitude changes led to relatively short wavelength variability in the pitch angle (approximately 2 s periodicity, Figure 7e). Interestingly, the bird's orientation seems to follow the pattern imposed by the towing helicopter without significant additional vibrations, demonstrating that the bird is relatively aerodynamically stable. Impor-

tantly, the resultant processed magnetic components and total field anomalies do not follow the periodic behavior of the three orientation angles, thereby confirming the reliability of the orientation data and the calibration and processing scheme. The observed total field anomalies were computed based on the three components measured by the vector magnetometer through the formula (Kontis and Young, 1964)

$$\mathrm{T} = (B_N - N)\cos D\cos I + (B_E - \mathrm{E})\sin D\cos I + (B_V - \mathrm{V})\sin I, \tag{5}$$

where D and I are the IGRF declination and inclination, respectively. The upward continued sea surface proton precession-derived total field anomalies (the red line in Figure 7d; Ben-Avraham et al., 2014) and our total field anomalies (the black line in Figure 7d) show a similar pattern. As expected for a north-striking magnetic boundary located at midlatitudes and a geomagnetic field declination of 5.2°, the amplitudes of the vertical component anomalies are approximately 30% larger than those of the total field anomalies (Gee and Cande, 2002).

The vector component data can be assessed for self-consistency by testing whether the power spectral density (PSD) of the vertical anomalies is equal to the sum of the PSDs of the two horizontal anomalies (i.e., "power sum rule," Parker and O'Brien, 1997). We applied this test to the entire data set (before upward continuation and filtering were done) and found an excellent agreement for wavenumbers smaller than 2.2 km^{-1}, corresponding to wavelengths longer than 0.45 km (Figure 8). This analysis suggests that the geologically related signal resides in wavelengths longer than 0.45 km and that wavelengths smaller than 0.45 km are most likely contaminated by the orientation errors of the towed bird. We have, therefore, assigned a low-pass filtering of 400 m.

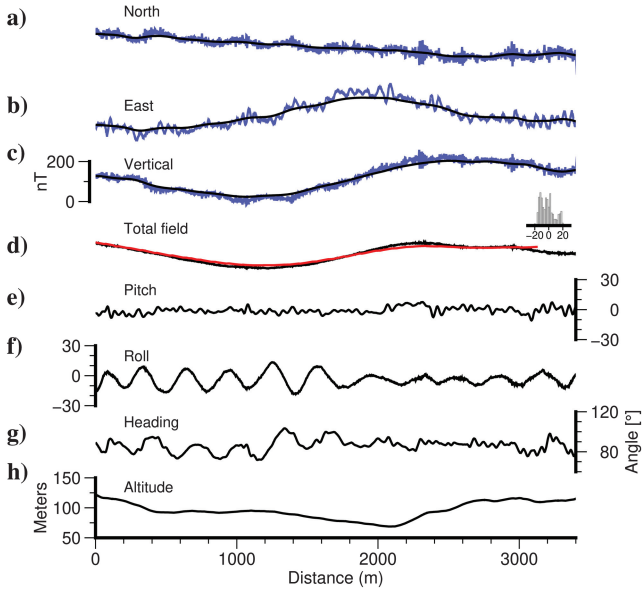

Figure 7. Results from a representative profile (the location of the profile is shown in Figure 10, Profile AA′). (a–c) The three magnetic components (blue lines) and (d) total field anomalies presented after calibration, compensation, rotation to geographical coordinates, and IGRF correction are applied. The vector anomalies marked by black lines in (a–c) are the same data, respectively, after they were upward continued to 135 m above the surface. The red line in (d) marks the offshore upward continued sea surface total field anomalies collected along the same profile (Ben-Avraham et al., 2014). The histogram on the right in (d) illustrates the differences between these sea surface data and our total field data. The three calibrated (for misalignment) orientation angles are shown in (e–g), respectively, and the altitude above the surface is shown in (h).

Our gridded total field and vector component anomalies are shown in Figure 9. The calculated RMSE of the crossover differences for the $B_N/B_E/B_V$ components are 24.7/88.9/19.8 nT, respectively. Leveling reduced the misfit to 15.6/44.5/14.0 nT, with the errors normally distributed around zero (Figure 9j). The total field anomalies have crossover differences (i.e., the noise level) of 7.1 nT before leveling and 4.8 nT after leveling, and they compare favorably with the upward continued sea surface total field anomalies (Ben-Avraham et al., 2014), with an overall standard deviation difference of 6.2 nT (Figure 9d and 9e).

In general, the land area is characterized by shorter-wavelength (500–1000 m) and high-amplitude anomalies, wherein the positive anomalies located in the northern part of the survey generally coincide with the exposures of basaltic flows (Figure 3b). In the lake area (Figures 9c, 9d, and 10), west of longitude 35.625°, the anomalies are characterized by intermediate (1.5–2 km) wavelengths, probably reflecting a longer distance between the magnetometer and the source layer (i.e., basalts). A north–south boundary that straddles longitude 35.625°, offshore and onshore, seems to divide the short wavelength signal (to the east) from the intermediate wavelength signal (to the west). As will be discussed subsequently in the text, this boundary follows the trace of the JGF as observed from seismic reflection profiles.

In general, the shape of the vertical anomalies (Figure 9c) follow the shape of the total field anomalies (Figure 9d), but the boundaries between the positive and negative anomalies of the vertical anomalies are sharper. The anomaly pattern of the data for the east component suffers from high-frequency variations (Figure 9b). This

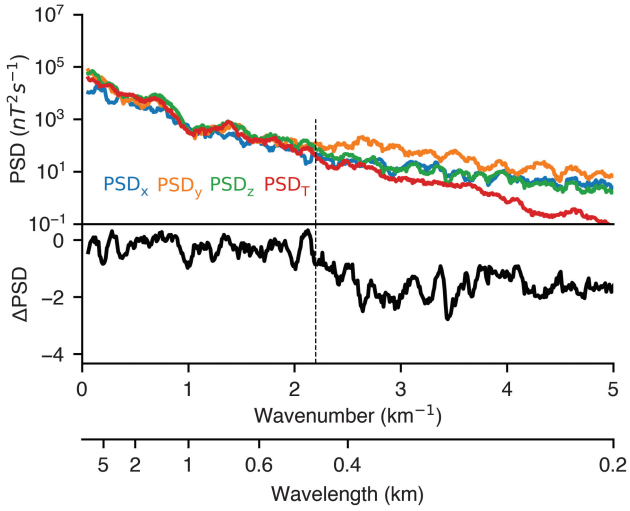

Figure 8. Power spectra density plots. Data from the entire survey were used and smoothed by averaging the estimates of 10 adjacent wavenumbers (five from both sides). The top panel shows the PSD of our calculated total field anomalies (PSD_T) and the vector components PSD_X, PSD_Y, and PSD_Z. The lower panel shows the difference between $\log(PSD_Z)$ and $\log(PSD_X + PSD_Y)$, illustrating the power sum rule. The dashed vertical line highlights the wavenumber above which the power sum rule fails.

behavior is expected given the 0.08° uncertainty of the heading direction (Figure 2b).

DISCUSSION

Quality of data

The quality of the data produced by the new vector magnetometer system can be assessed internally by analyzing the noise levels and externally by comparing the total field anomalies against the previously collected sea surface anomalies. The total field noise level (4.8 nT, Figure 9j) of the AeroVmag system obtained for 255 crossover points (Figure 9d) is comparable to the typical 2–6 nT error level achieved by the stinger tale and wing-tips magnetometer systems (e.g., Munschy and Fleury, 2011; Coyle et al., 2014). The three component anomalies pass the power sum rule for wavelengths longer than approximately 450 m, indicating that the orientation noise dominated the signal at shorter wavelengths. The estimated noise levels of the filtered component data (15.6/44.5/14.0 nT for $B_N/B_E/B_V$) are similar to the theoretical noise levels predicted by considering the orientation uncertainties and characteristics of the local geomagnetic field (18.1/45.1/15.7 nT for $B_N/B_E/B_V$, Figure 2). This consistency indicates that other sources do not introduce significant magnetic noise.

The lack of preexisting vector magnetic data prevents us from directly comparing our vectorial results with previous studies. However, the total field anomalies calculated from the component data (Figure 9d) can be compared against the upward continued sea surface total field anomalies previously collected by a ship-towed proton precession magnetometer (Ben-Avraham et al., 2014; Figure 9e). Because the magnetic source layer is relatively thin (an approximately 200 m thick volcanic unit; Sneh et al., 1998), has moderate natural remanent magnetization values (10^0–10^1 A/m), and has Konigsberger ratios of approximately 10 (Dembo et al., 2021), the two data sets should provide similar results. In general, the two data sets reflect similar anomaly patterns with a standard deviation difference of 6.2 nT between our total field anomaly and the upward continued sea surface data. The noise that was computed based on the 255 crossover differences indicates that, overall, the data are internally consistent, while the comparison with the sea surface total field

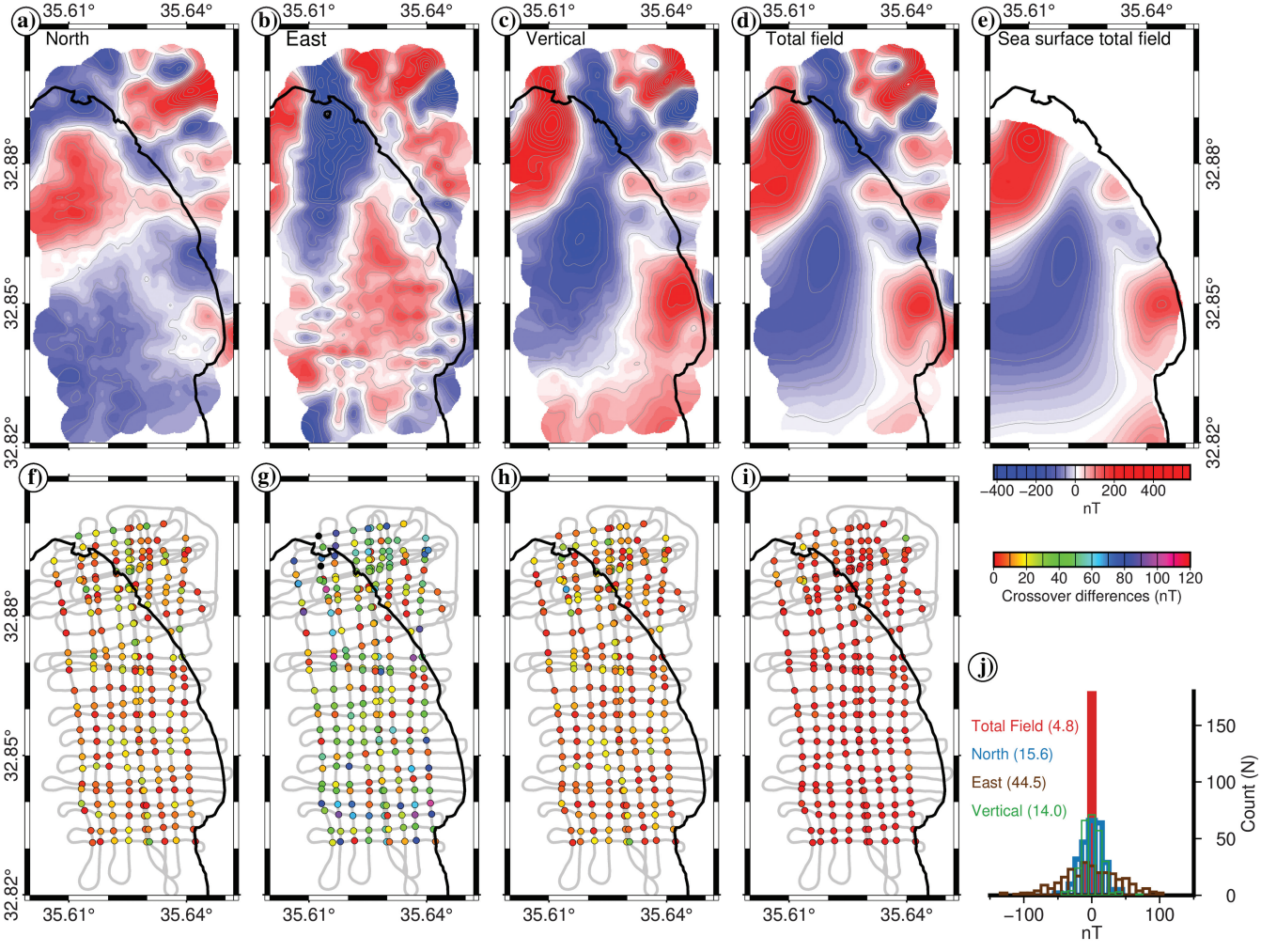

Figure 9. Magnetic anomaly maps of the (a) north, (b) east, and (c) vertical magnetic components, (d) the total field, and (f–i) the corresponding crossover differences. (e) Upward continued sea surface total field anomalies (Ben-Avraham et al., 2014). In all maps, the black line marks the location of the coastline. (j) The distribution of the 255 crossover differences shown in (f–i). The grids were prepared by block-mean filtering (cell size = 20 m) and gridding using generic mapping tools software (Wessel et al., 2019).

anomalies provides external validation for our results and, therefore, for the AeroVmag system.

Tectonic implications

The architecture of the Dead Sea Fault system within and near the Sea of Galilee is still a hotly debated topic (e.g., Gasperini et al., 2020; Dembo et al., 2021; ten Brink et al., 2023). In particular, one of the key open questions related to the structure of the Dead Sea Fault system is how the offshore East Marginal Fault that straddles the east coast of the Sea of Galilee is connected to the onshore JGF located north of the lake (Figure 3). Direct constraints on the fault architecture are given by the relatively sparse available seismic reflection profiles (Figure 10). Additional constraints are given by the available, total field magnetic anomalies that cover the deeper (depths >5 m) parts of the lake (Ben-Avraham et al., 2014) and a few onshore magnetic profiles (Schattner et al., 2019). Our extended data coverage allows us to connect the offshore and onshore faults with more confidence. The reduced to the pole vertical component anomalies (Figure 10) and total field anomalies (Figure 9) show a prominent north–south magnetic contrast (longitude 35.625°, marked by the thick black line in Figure 10) that bounds the rather short wavelength anomalies on the east from the longer wavelength anomalies on the west. This boundary is located due south of the north–south JGF that cuts the Pleistocene basalts and forms the Jordan Gorge cliff (Garfunkel et al., 1981). The seismic reflection profile K-03 (Figures 10 and 11; Hurwitz et al., 2002) shows that the north–south magnetic contrast is located above a prominent fault that dips westward and throws the western hanging wall downward for approximately 800 m. The longer distance between the magnetic measurement level and the source layer west of the fault, relative to the shorter distance east of the fault, may explain the general trend of the longer wavelength anomalies found west of the fault compared with the anomalies found east of the fault. The exact position of the southern edge of the fault is unclear. The fault is not imaged along the K-04 seismic profile (for the position, please see Figure 10), and the sharp magnetic contrast that follows the trace of the fault seems to vanish southward (Figure 10). Therefore, we suggest that the southern edge of the fault is located slightly southward of where the seismic profile K-03 intersects the fault.

In the northern part of the survey area, the JGF is buried under Holocene alluvium and deltaic sediments in the northern coast area of the lake, but it could be traced on seismic line GI-3591 as a complex and wide (a few hundred meters) fault zone (Rotstein and Bartov, 1989). Our results agree with the model proposed by Hurwitz et al. (2002), confirming that the JGF runs southward into the offshore area without any major segmentation. This inference is supported by onshore paleomagnetic rotations and mechanical modeling (Dembo et al., 2021), which suggest that no stepover was located in the northern part of the lake. According to seismic profile K-03 (Figure 11), under the limitation of profile resolution, the fault is covered by an uninterrupted sequence of sediments. Thus, it seems that the activity along this trace of the JGF has recently slowed down or even been abandoned. A paleoseismic trench study (Marco et al., 2005) indicated that the active fault segment is currently located approximately 200 m west (the red line in Figure 10) of where we interpret the fault to exist, but still within

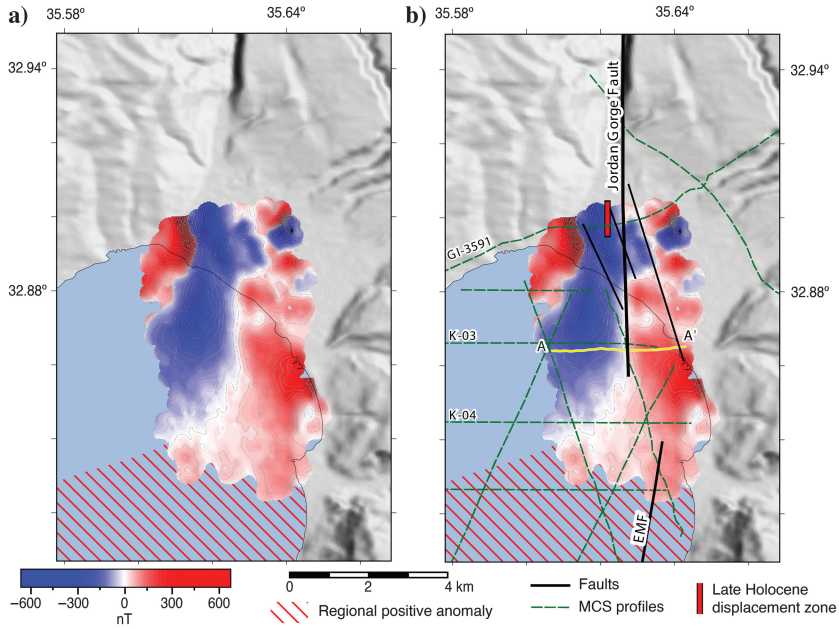

Figure 10. (a) The uninterpreted and (b) interpreted, reduced to the pole (Ueda et al., 2013), vertical component anomaly grid projected over the topography map. The location of the previously collected multichannel seismic reflection profiles is highlighted by green dashed lines (Rotstein and Bartov, 1989; Hurwitz et al., 2002). The thick black lines indicate the fault traces' locations confirmed by seismic reflection data. The thin black lines show the location of the suspected secondary faults, based on our magnetic data. The Late Holocene displacement zone observed in paleoseismological trenches is shown with a red line (Marco et al., 2005). Line AA′ marks the location of the magnetic profile shown in Figures 7 and 11. The East Marginal Fault follows the position defined by Hurwitz et al. (2002). The red shading shows the northern extent of the prominent positive magnetic anomaly (Ben-Avraham et al., 2014).

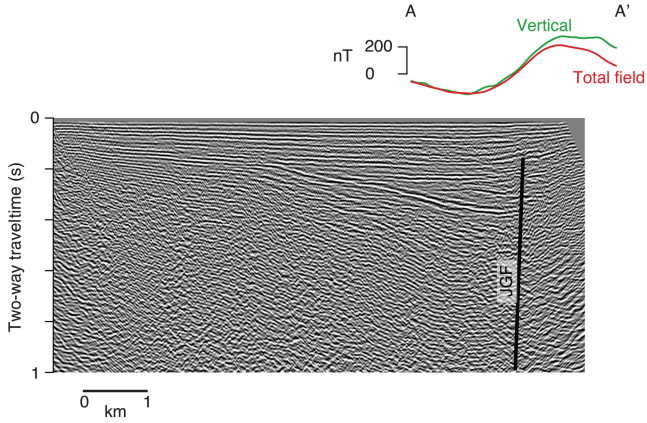

Figure 11. Seismic line K-03 (Hurwitz et al., 2002) and the reduced to the pole vertical and total field anomalies (profile A-A′, Figure 10). The position of the JGF is marked by a thick black line.

the wide fault zone of the JGF as imaged by Rotstein and Bartov (1989). Ten Brink et al. (2023) suggest that these different positions could indicate that this fault has migrated to its current more westerly position relatively recently and that most of the displacement within the northern part of the lake has been accommodated along the main north–south JGF strand. Finally, our data show secondary lineations oriented in an approximately 340°–160° direction. We interpret these linear features as secondary young en-echelon faults (marked by the thin black lines in Figure 10b) that cross the seismic line GI-3591 at the position of the wide fault zone of the JGF.

Unlike the JGF, the East Marginal Fault, imaged by seismic reflection profiles and gravity data (Reznikov et al., 2004; Gasperini et al., 2020; ten Brink et al., 2023), is not accompanied by a magnetic anomaly (Figure 10). A rather large, positive magnetic anomaly dominates the central and eastern parts of the lake (Ben-Avraham et al., 2014) and seems to originate from the magnetization of the river-derived sediments deposited there. This large positive anomaly seems to mask the magnetic-related signal of the East Marginal Fault, and therefore, our results do not add new constraints to the exact location of the East Marginal Fault.

Applicability of the AeroVmag magnetometer system

Measuring the three components of the anomalous magnetic field provides several benefits compared with the traditional total field magnetic observations. For instance, the amplitudes of the anomalous components (horizontal or vertical components) are enhanced at low latitudes or when the source layer is magnetized with a shallow inclination angle. Furthermore, the vector anomalies provide, even with a single profile, constraints on the dimensionality and orientation of the source layer, thus allowing for the investigation of various geodynamical phenomena (e.g., crustal structure, geomagnetic field behavior, etc.) with minimal data collection. However, the noise levels of our system (up to 20 nT for the vertical component and up to 50–70 nT for the north and east components, Figure 2) are difficult to eliminate because they arise due to uncertainties related to the orientation. Nevertheless, the system has a clear advantage over the ship-towed vector magnetometers that have no heading constraints, and thus, they provide only the horizontal and vertical components of the anomalous fields. Furthermore, the available platform-mounted aerial and shipboard vector magnetometers suffer from noises related to the orientation uncertainties and magnetic contamination induced by the temporally varying magnetization of the carrying platforms (either induced and/or permanent). Therefore, our system is expected to be useful in areas where the anomalous field is stronger than approximately 100 nT and has typical wavelengths longer than the wavelengths related to the orientation noise. Thus, the velocities at which the survey is conducted, the distance above the magnetic source layer, and the atmospheric conditions govern the range of detectable wavelengths. In general, we expect the system to be most useful for regional surveys when studying crustal-scale phenomena (such as marine magnetic anomalies and continental plate boundaries). Expected improvements in future orientation sensors will reduce the noise levels of the three magnetic components, thereby opening new avenues for applications, for instance, detecting weak and short-wavelength anomalous fields, such as those produced by unexploded ordnance or relatively small geologic features.

CONCLUSION

We present the AeroVmag, a new aero-towed vector magnetometer system that can be towed by either rotary- or fixed-wing aircraft. We validated the system using data collected during a test survey conducted over and near the northeastern part of the Sea of Galilee. Evaluation of 255 crossover points revealed noise levels of 4.7 nT for the total field anomaly data, results that are comparable to the existing aeromagnetic total field systems that are installed on the carrying platforms. The results also suggest that the noise from the three magnetic components arises only from the uncertainties of the orientation sensor and that it accounts for <45 nT noise levels. Our data compare favorably with the existing sea surface total field anomaly data. The trace of the major north–south magnetic boundary imaged by our data spatially coincides with the seismically imaged location of the JGF, which cuts through the northeast part of the basin.

The quality of the three magnetic components is within the acceptable thresholds for a broad range of regional applications, especially those involving equatorial investigations and those wherein the magnetic source layer is hidden (e.g., under ice or vegetation). The main limitation of our system is dictated by the accuracy of the orientation information. Expected improvements in future orientation sensors will, therefore, improve the accuracy of the three magnetic components produced by our system.

ACKNOWLEDGMENTS

We would like to thank R. Edut for his excellent assistance in building and maintaining the system. We also thank the pilot, A. Hachmon, for his great support during the survey. We thank the associate editor, the reviewer, G. Phelps, and the anonymous reviewer for their constructive and valuable comments that improved the paper significantly.

DATA AND MATERIALS AVAILABILITY

Data associated with this research are available and can be accessed via the following URL: https://zenodo.org/records/10654125.

REFERENCES

Alken, P., E. Thébault, C. D. Beggan, H. Amit, J. Aubert, J. Baerenzung, T. N. Bondar, W. J. Brown, S. Califf, A. Chambodut, A. Chulliat, G. A. Cox, C. C. Finlay, A. Fournier, N. Gillet, A. Grayver, M. D. Hammer, M. Holschneider, L. Huder, G. Hulot, T. Jager, C. Kloss, M. Korte, W. Kuang, A. Kuvshinov, B. Langlais, J. M. Léger, V. Lesur, P. W. Livermore, F. J. Lowes, S. Macmillan, W. Magnes, M. Mandea, S. Marsal, J. Matzka, M. C. Metman, T. Minami, A. Morschhauser, J. E. Mound, M. Nair, S. Nakano, N. Olsen, F. J. Pavón-Carrasco, V. G. Petrov, G. Ropp, M. Rother, T. J. Sabaka, S. Sanchez, D. Saturnino, N. R. Schnepf, X. Shen, C. Stolle, A. Tangborn, L. Toffner-Clausen, H. Toh, J. M. Torta, J. Varner, F. Vervelidou, P. Vigneron, I. Wardinski, J. Wicht, A. Woods, Y. Yang, Z. Zeren, and B. Zhou, 2021, International geomagnetic reference field: The thirteenth generation: Earth Planets and Space, **73**, 49, doi: 10.1186/s40623-020-01288-x.

Barckhausen, U., C. R. Ranero, S. C. Cande, M. Engels, and W. Weinrebe, 2008, Birth of an intraoceanic spreading center: Geology, **36**, 767–770, doi: 10.1130/G25056A.1.

Ben-Avraham, Z., M. Rosenthal, G. Tibor, H. Navon, H. Wust-Bloch, R. Hofstetter, and M. Rybakov, 2014, Structure and tectonic development of the Kinneret Basin: Lake Kinneret: Ecology and Management, **6**, 19–38.

Berrios-Rivera, N., J. S. Gee, R. Parnell-Turner, S. Maher, J. N. Wu, D. Fornari, M. Tivey, M. Marjanovic, T. Barreyre, and J. McDermott, 2023, Significance of short-wavelength magnetic anomaly low along

the East Pacific Rise axis, 9°50'N: Geochemistry Geophysics Geosystems, **24**, e2023GC010875, doi: 10.1029/2023GC010875.
Blakely, R. J., 1995, Potential theory in gravity and magnetic applications: Cambridge University Press.
Blakely, R. J., A. Cox, and E. J. Iufer, 1973, Vector magnetic data for detecting short polarity intervals in marine magnetic profiles: Journal of Geophysical Research, **78**, 6977–6983, doi: 10.1029/JB078i029p06977.
Coleman, R. J., 1992, Project Magnet high-level vector survey data reduction, *in* R. A. Langel and R. T. Baldwin, eds., Types and characteristics of data for geomagnetic field modeling: Nasa Conference Publications No. 3153, 215–248.
Coyle, M., R. Dumont, P. Keating, F. Kiss, and W. Miles, 2014, Geological Survey of Canada aeromagnetic surveys: Design, quality assurance, and data dissemination: Geological Survey of Canada.
Dembo, N., Y. Hamiel, and R. Granotaaaa, 2021, The stepovers of the Central Dead Sea Fault: What can we learn from the confining vertical axis rotations? Tectonophysics, **816**, 229036, doi: 10.1016/j.tecto.2021.229036.
Dransfield, M., A. Christensen, and G. M. Liu, 2003, Airborne vector magnetics mapping of remanently magnetized banded iron formations at Rocklea, Western Australia: Exploration Geophysics, **34**, 93–96, doi: 10.1071/EG03093.
Engels, M., U. Barckhausen, and J. S. Gee, 2008, A new towed marine vector magnetometer: methods and results from a Central Pacific cruise: Geophysical Journal International, **172**, 115–129, doi: 10.1111/j.1365-246X.2007.03601.x.
Eppelbaum, L. V., Z. Ben-Avraham, and Y. Katz, 2007, Structure of the Sea of Galilee and Kinarot Valley derived from combined geological geophysical analysis: First Break, **25**, 43–50, doi: 10.3997/1365-2397.2007001.
Farr, T. G., P. A. Rosen, E. Caro, R. Crippen, R. Duren, S. Hensley, M. Kobrick, M. Paller, E. Rodriguez, L. Roth, D. Seal, S. Shaffer, J. Shimada, J. Umland, M. Werner, M. Oskin, D. Burbank, and D. Alsdorf, 2007, The shuttle radar topography mission: Reviews of Geophysics, **45**, RG2004, doi: 10.1029/2005RG000183.
Garfunkel, Z., I. Zak, and R. Freund, 1981, Active faulting in the Dead-Sea rift: Tectonophysics, **80**, 1–26, doi: 10.1016/0040-1951(81)90139-6.
Gasperini, L., M. Lazar, A. Mazzini, M. Lupi, A. Haddad, C. Hensen, M. Schmidt, A. Caracausi, M. Ligi, and A. Polonia, 2020, Neotectonics of the Sea of Galilee (northeast Israel): implication for geodynamics and seismicity along the Dead Sea Fault system: Scientific Reports, **10**, 11932, doi: 10.1038/s41598-020-67930-6.
Gee, J. S., and S. C. Cande, 2002, A surface-towed vector magnetometer: Geophysical Research Letters, **29**, 15-1–15-4, doi: 10.1029/2002GL015245.
Gee, J. S., and D. V. Kent, 2007, Source of oceanic magnetic anomalies and the geomagnetic polarity timescale, *in* M. Kono, ed., Treatise on geophysics, vol. 5: Elsevier, 455–507.
Granot, R., 2016, Palaeozoic oceanic crust preserved beneath the eastern Mediterranean: Nature Geoscience, **9**, 701–705, doi: 10.1038/ngeo2784.
Guspí, F., 1987, Frequency-domain reduction of potential-field measurements to a horizontal plane: Geoexploration, **24**, 87–98, doi: 10.1016/0016-7142(87)90083-4.
Hamiel, Y., and O. Piatibratova, 2023, Transient behavior and interplay between seismic and aseismic deformation near the tip of a creeping segment: Insights from the Northern Jordan Valley segment of the Dead Sea Fault: Geophysical Research Letters, **50**, e2022GL100584, doi: 10.1029/2022GL100584.
Hamiel, Y., O. Piatibratova, and Y. Mizrahi, 2016, Creep along the northern Jordan Valley section of the Dead Sea Fault: Geophysical Research Letters, **43**, 2494–2501, doi: 10.1002/2016GL067913.
Hinze, W. J., R. R. B. von Frese, and A. H. Saad, 2013, Gravity and magnetic exploration: Principles, practices, and applications: Cambridge University Press.
Honsho, C., T. Ura, and K. Kim, 2013, Deep-sea magnetic vector anomalies over the Hakurei hydrothermal field and the Bayonnaise knoll caldera, Izu-Ogasawara arc, Japan: Journal of Geophysical Research, **118**, 5147–5164, doi: 10.1002/jgrb.50382.
Horner-Johnson, B. C., and R. G. Gordon, 2003, Equatorial Pacific magnetic anomalies identified from vector aeromagnetic data: Geophysical Journal International, **155**, 547–556, doi: 10.1046/j.1365-246X.2003.02065.x.
Hurwitz, S., Z. Garfunkel, Y. Ben-Gai, M. Reznikov, Y. Rotstein, and H. Gvirtzman, 2002, The tectonic framework of a complex pull-apart basin: seismic reflection observations in the Sea of Galilee, Dead Sea transform: Tectonophysics, **359**, 289–306, doi: 10.1016/S0040-1951(02)00516-4.
Isezaki, N., 1986, A new shipboard 3-component magnetometer: Geophysics, **51**, 1992–1998, doi: 10.1190/1.1442054.
Isezaski, N., and J. Matsuo, 2009, Magnetization structure of Aogashima Island using vector magnetic anomalies obtained by a helicopter-borne magnetometer: Exploration Geophysics, **40**, 17–26, doi: 10.1071/EG08112.
Jekeli, C., 2023, Inertial navigation systems with geodetic applications: Walter de Gruyter.
Kato, H., N. Isezaki, C. H. Park, C. H. Kim, and M. Nakanishi, 2007, Characteristics of crustal magnetic structures in the Tsushima (Ulleung) and Japan Basins from vector magnetic anomalies: Earth Planets and Space, **59**, 887–895, doi: 10.1186/BF03352751.
Kontis, A. L., and G. A. Young, 1964, Approximation of residual total-magnetic-intensity anomalies: Geophysics, **29**, 623–627, doi: 10.1190/1.1439400.
Korenaga, J., 1995, Comprehensive analysis of marine magnetic vector anomalies: Journal of Geophysical Research, **100**, 365–378, doi: 10.1029/94JB02596.
Marco, S., T. K. Rockwell, A. Heimann, U. Frieslander, and A. Agnon, 2005, Late Holocene activity of the Dead Sea Transform revealed in 3D palaeoseismic trenches on the Jordan Gorge segment: Earth and Planetary Science Letters, **234**, 189–205, doi: 10.1016/j.epsl.2005.01.017.
Munschy, M., D. Boulanger, P. Ulrich, and M. Bouiflane, 2007, Magnetic mapping for the detection and characterization of UXO: Use of multi-sensor fluxgate 3-axis magnetometers and methods of interpretation: Journal of Applied Geophysics, **61**, 168–183, doi: 10.1016/j.jappgeo.2006.06.004.
Munschy, M., and S. Fleury, 2011, Scalar, vector, tensor magnetic anomalies: measurement or computation? Geophysical Prospecting, **59**, 1035–1045, doi: 10.1111/j.1365-2478.2011.01007.x.
Nabighian, M. N., V. J. S. Grauch, R. O. Hansen, T. R. LaFehr, Y. Li, J. W. Peirce, J. D. Phillips, and M. E. Ruder, 2005, 75th Anniversary — The historical development of the magnetic method in exploration: Geophysics, **70**, no. 6, 33ND–61ND, doi: 10.1190/1.2133784.
Nogi, Y., and K. Kaminuma, 1999, Measurements of vector magnetic anomalies on board the icebreaker Shirase and the magnetization of the ship: Annali Di Geofisica, **42**, 161–170, doi: 10.4401/ag-3711.
Nuriel, P., R. Weinberger, A. R. C. Kylander-Clark, B. R. Hacker, and J. P. Craddock, 2017, The onset of the Dead Sea transform based on calcite age-strain analyses: Geology, **45**, 587–590, doi: 10.1130/G38903.1.
Olsen, N., T. Risbo, P. Brauer, J. Merayo, F. Primdahl, and T. Sabaka, 2001, In-flight calibration methods used for the Ørsted Mission, ESA-SP on calibration of magnetometers, (Vol. 22): Technical University of Denmark.
Pang, H. F., Q. Zhang, J. Li, S. T. Luo, D. X. Chen, M. C. Pan, and F. L. Luo, 2014, Improvement of vector compensation method for vehicle magnetic distortion field: Journal of Magnetism and Magnetic Materials, **353**, 1–5, doi: 10.1016/j.jmmm.2013.10.015.
Parker, R. L., and M. S. O'Brien, 1997, Spectral analysis of vector magnetic field profiles: Journal of Geophysical Research, **102**, 24815–24824, doi: 10.1029/97JB02130.
Prince, R. A., and D. W. Forsyth, 1984, A simple objective method for minimizing crossover errors in marine gravity data: Geophysics, **49**, 1070–1083, doi: 10.1190/1.1441722.
Reznikov, M., Z. Ben-Avraham, Z. Garfunkel, H. Gvirtzman, and Y. Rotstein, 2004, Structural and stratigraphic framework of Lake Kinneret: Israel Journal of Earth Sciences, **53**, 131–149, doi: 10.1560/QY1W-VVRM-FLNK-C9M9.
Rigoti, A., A. L. Padilha, F. H. Chamalaun, and N. B. Trivedi, 2000, Effects of the equatorial electrojet on aeromagnetic data acquisition: Geophysics, **65**, 553–558, doi: 10.1190/1.1444750.
Rotstein, Y., and Y. Bartov, 1989, Seismic reflection across a continental transform — An example from a convergent segment of the Dead-Sea Rift: Journal of Geophysical Research, **94**, 2902–2912, doi: 10.1029/JB094iB03p02902.
Schattner, U., A. Segev, V. Mikhailov, M. Rybakov, and V. Lyakhovsky, 2019, Magnetic signature of the Kinneret-Kinarot Tectonic Basin along the Dead Sea Transform, Northern Israel: Pure and Applied Geophysics, **176**, 4383–4399, doi: 10.1007/s00024-019-02211-6.
Seama, N., Y. Nogi, and N. Isezaki, 1993, A new method for precise determination of the position and strike of magnetic boundaries using vector data of the geomagnetic anomaly field: Geophysical Journal International, **113**, 155–164, doi: 10.1111/j.1365-246X.1993.tb02536.x.
Seton, M., J. M. Whittaker, P. Wessel, R. D. Müller, C. DeMets, S. Merkouriev, S. Cande, C. Gaina, G. Eagles, R. Granot, J. Stock, N. Wright, and S. E. Williams, 2014, Community infrastructure and repository for marine magnetic identifications: Geochemistry Geophysics Geosystems, **15**, 1629–1641, doi: 10.1002/2013GC005176.
Sneh, A., Y. Bartov, T. Weissbrod, and M. Rosensaft. 1998, Geological map of Israel, 1:200,000: Geological Survey of Israel.
ten Brink, U. S., E. Levi, C. H. Flores, I. Koulakov, N. Bronshtein, and Z. Ben-Avraham, 2023, Crustal structure across the Central Dead Sea Transform and surrounding areas: insights into tectonic processes in continental transforms: Tectonics, **42**, e2023TC007799, doi: 10.1029/2023TC007799.
Uieda, L., V. C. Oliveira, Jr, and V. C. F. Barbosa, 2013, Modeling the earth with Fatiando a Terra: Proceedings of the 12th Python in Science Conference, 91–98.
Wessel, P., J. F. Luis, L. Uieda, R. Scharroo, F. Wobbe, W. H. F. Smith, and D. Tian, 2019, The generic mapping tools version 6: Geochemistry Geophysics Geosystems, **20**, 5556–5564, doi: 10.1029/2019GC008515.

Xie, R. K., S. Q. Xiong, S. L. Duan, J. L. Wang, P. Wang, Y. Luo, H. J. Liu, and Z. G. Fan, 2020, Noise estimation in vector magnetic data derived from airborne vector magnetic system: Geophysics, **85**, no. 4, J71–J83, doi: 10.1190/geo2019-0663.1.

Yamamoto, M., N. Seama, and N. Isezaki, 2005, Geomagnetic paleointensity over 1.2 Ma from deep-tow vector magnetic data across the East Pacific Rise: Earth Planets and Space, **57**, 465–470, doi: 10.1186/BF03351835.

Yamazaki, Y., and A. Maute, 2017, Sq and EEJ — A review on the daily variation of the geomagnetic field caused by ionospheric dynamo currents: Space Science Reviews, **206**, 299–405, doi: 10.1007/s11214-016-0282-z.

Yang, J. H., S. Liu, and X. Y. Hu, 2020, Inversion of high-amplitude magnetic total field anomaly: An application to the Mengku iron-ore deposit, northwest China: Scientific Reports, **10**, 11949, doi: 10.1038/s41598-020-68494-1.

Biographies and photographs of the authors are not available.